PS-*b*-P4VP block copolymer micelles as a soft template to grow openly porous nickel films for alkaline hydrogen evolution

Roberto Fagotto Clavijo [a], Marta Riba-Moliner [b], Arántzazu González-Campo [b], Jordi Sort [a,c], Eva Pellicer [a,*], Konrad Eiler [a,*]

[a] *Departament de Física, Universitat Autònoma de Barcelona, 08193 Bellaterra, Spain*
[b] *Institut de Ciència de Materials de Barcelona (ICMAB-CSIC), 08193 Bellaterra, Spain*
[c] *Institució Catalana de Recerca i Estudis Avançats (ICREA), Pg. Lluís Companys 23, 08010 Barcelona, Spain*

A B S T R A C T

Highly porous Ni films have been potentiostatically synthesised by micelle-assisted electrodeposition using custom-made PS-*b*-P4VP block copolymer micelles as a soft template. Two PS-*b*-P4VP block copolymers with PS/P4VP block ratios of 1:1 and 1:4 were used for the micelle-assisted electrodeposition, resulting in Ni films with large pores of diameters varying from 25 to 600 nm (1:1), and from 10 to 230 nm (1:4). As a result of the interconnected porosity, and hence the drastic increase of the surface-to-volume ratio, the electrocatalytic performance at hydrogen evolution reaction (HER) in alkaline media is significantly improved in comparison to a dense Ni film, and—more importantly—even in comparison to a highly mesoporous Ni film with monodisperse 10 nm wide pores. Most remarkably, it is discovered that the openly porous Ni electrocatalysts not only lead to a simple increase in HER current density, but also to a lower overpotential and a better long-term performance. While the bulk of the films is metallic, $Ni(OH)_2$ is formed on the surfaces of all Ni films during HER. This effect leads to an initial decrease of the catalytic activity, but provides excellent stability in alkaline media. The presented synthesis process for pure Ni may be readily adopted to any other electroplatable metals and alloys.

1. Introduction

Current global challenges, such as the climate crisis, demand for technological advances towards more efficient and sustainable energy management. In order to decrease the use of fossil fuels, changes in infrastructure, energy storage, and energy production are required [1]. In a future low-carbon economy, hydrogen energy will play a major role due to its high versatility and ability to provide energy for the transportation, storage, and domestic energy applications in today's society [2].

One of the most promising and emission-free means of energy storage and production is through eletrolyser and fuel cell technologies [3]. Making use of the hydrogen evolution reaction (HER) as an electrocatalytic process, green hydrogen can be produced emission-free when the required electric current is obtained by renewable energies [4].

Nanostructured materials have shown tremendous impact on fostering the development of electrolysers and fuel cells towards commercialisation. While platinum-based catalysts are the most

electrochemically active materials for low temperature hydrogen fuel cells, its cost is extremely high due to its low abundance. Alternative materials are being investigated to make catalysts more accessible and affordable [5]. Recent studies have shown that by partially substituting platinum by an electrocatalytically active transition metal such as nickel, the cost-effectiveness may increase [6]. Furthermore, the nanostructuring of electrocatalysts, such as by application of porous materials, adds up to the efficiency by increase of the surface-to-volume ratio (S/V) [7]. Micelle-assisted electrodeposition has proven to render high-quality mesoporous materials in a rather simple synthesis process. Micelles are formed by block copolymers (BCP) in an aqueous electrolyte above critical micelle concentration. The micelles codeposit together with the discharged metal ions, leaving spherical pores in the electroplated metal or alloy once the polymer is dissolved [8].

Recently, highly mesoporous Ni-Pt thin films with a pore size of 10 nm have shown an improvement of HER activity with respect to fully dense films, however, the electrocatalytic activity did not increase as much as could be anticipated from the high porosity [9]. One possible
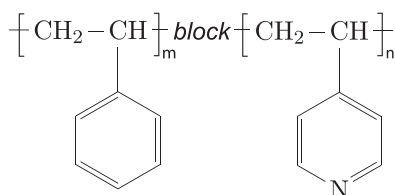

Fig. 1. Chemical structure of PS-*b*-P4VP.

Table 1
Amounts of initiator, styrene, and 4-vinylpyridine used in the synthesis of the PS-*b*-P4VP block copolymers.

Molar ratio	Initiator amount (mmol)	Styrene amount (mmol)	4-vinylpyridine amount (mmol)
1:1	61	40	40
1:4	36	17	63

explanation is that the pore size was not sufficiently large such as for an aqueous electrolyte to effectively penetrate the pores, although the surface energy did not increase due to the porosity. Secondly, the formed hydrogen gas bubbles may become trapped inside the pores, or block these, leading to a reduction of the available surface area. It was hypothesised that if the size of the hydrogen bubbles resulting from proton reduction was much larger than the actual size of the pores, the latter would not be efficiently utilised. Indeed, formed hydrogen bubbles are usually much larger than 10 nm before released from the surface [10]. Another critical point is the presence of an open or a closed porosity; if the porosity is closed then the electrocatalytic processes are limited to the surface without taking advantage of the sub-surface porous structure. On the other hand, an entirely open porosity would theoretically allow to make use of the entire structure in electrocatalysis. Furthermore, porous structures may significantly alter the wetting behaviour of surfaces, which needs to be monitored [11].

Nickel and its alloys, such as commercial Raney Ni, are generally promising candidates for HER in alkaline and neutral electrolytes [12–16], as well as for various other electrocatalytic reactions [17,18]. In contrast to acidic electrolysis, alkaline hydrogen evolution does not require the use of platinum group metals indeed [19]. Apart from metallic Ni-based electrocatalysts, nickel oxides, hydroxides and phosphides may be equally active [20–23].

Considering the aforementioned points, the goal of this work is to synthesise a HER electrocatalyst with an open porosity, and a pore size

that is significantly higher than the previously mentioned 10 nm, by micelle-assisted electrodeposition. Most commercial micelle-forming BCP, including Pluronic P-123, F-127 or Brij-56, have relatively low molecular weight, facilitating the spontaneous micelle formation in aqueous media, but therefore also form relatively small micelles, leading to rather small pore sizes when used in micelle-assisted synthesis methods [24]. Larger BCPs with high molecular weight do not form micelles spontaneously; in this case the micelles need to be stabilised in a multi-step process as described by Nagarajan on the example of PS-*b*-PEO [25].

Experimentally, only few studies have focussed on the synthesis of porous metals using high molecular weight BCP micelles. Yamauchi et al. prepared mesoporous Pt particles from a lyotropic liquid crystal (LLC) phase of PS_{3800}-*b*-PEO_{4800}, resulting in homogeneously porous particles with a pore size of 15 nm [26]. Later, higher molecular weight PS_{63000}-*b*-PEO_{26000} was used for electrodeposition of mesoporous Ni and Cu films, and yielded a pore size of around 50 nm [27,28]. The same BCP was used by Artal et al. for the electrodeposition of Ni-Pt alloy films, achieving a uniform pore size of approx. 30 nm [29]. Usually, the solvent exchange method is used, where the BCP is at first dissolved in a non-selective medium such as tetrahydrofurane (THF), before a selective
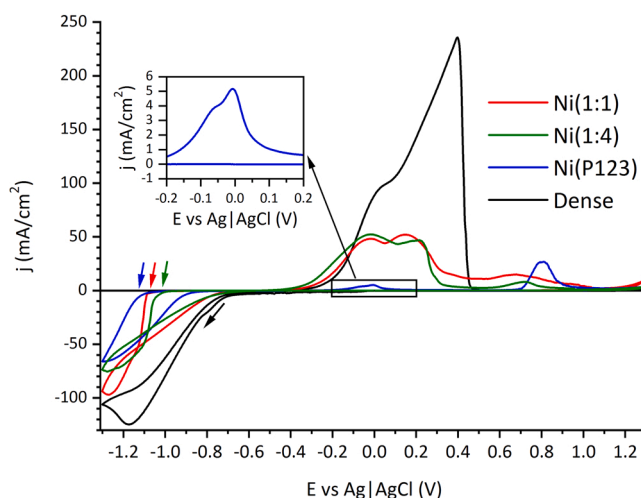

Fig. 3. CV curves recorded from the electrolytes used for the synthesis of dense Ni, Ni(P123), Ni(1:1), and Ni(1:4). Arrows indicate the onset of reduction as well as the scan direction.
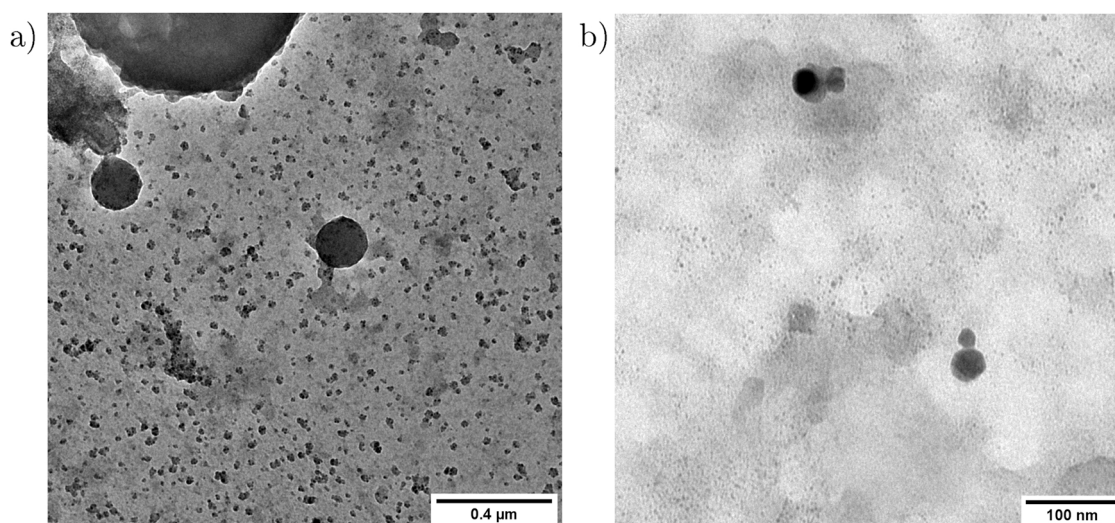

Fig. 2. TEM micrographs showing PS-*b*-P4VP micelles with block ratios 1:1 (a) and 1:4 (b).
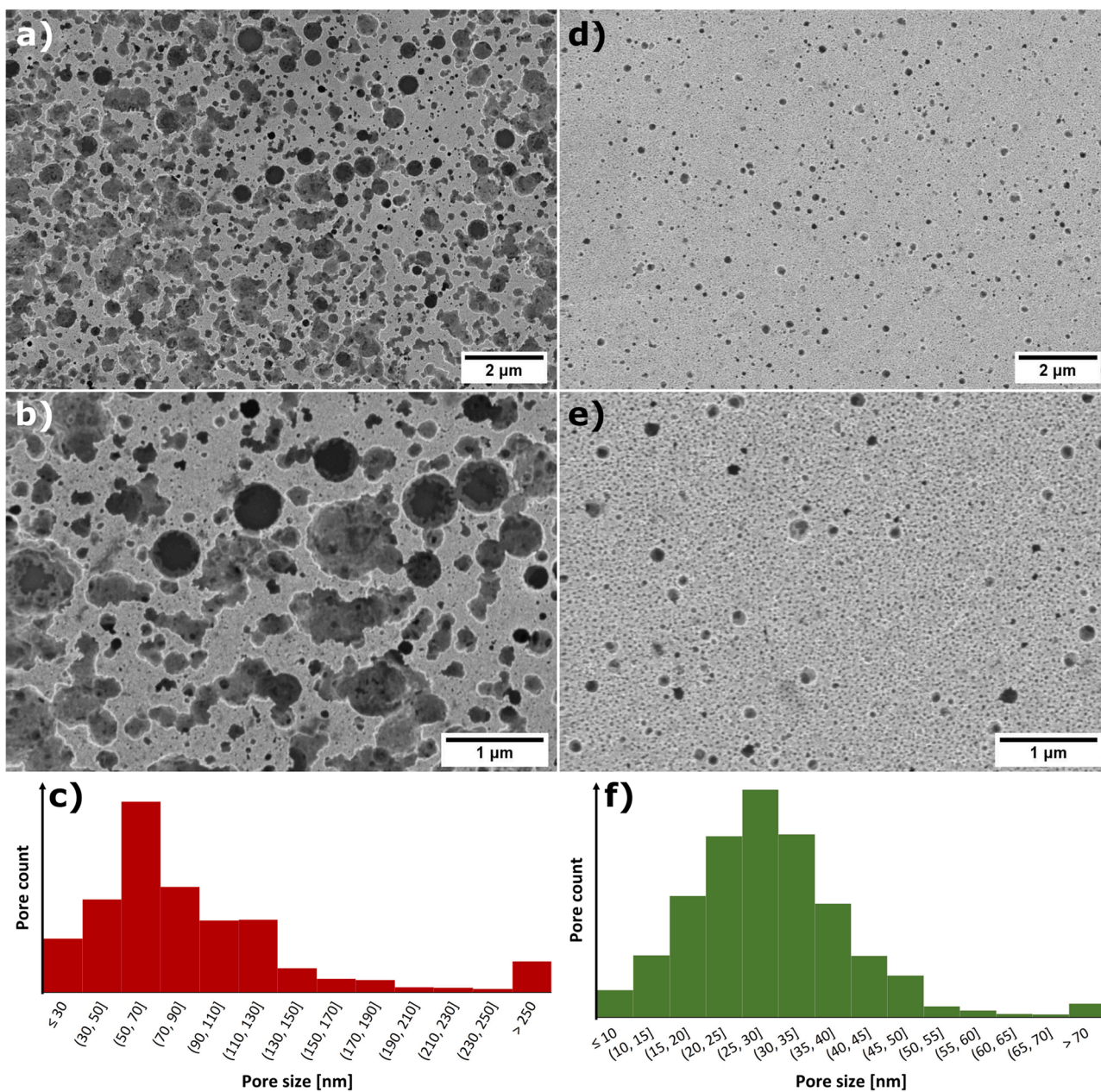
Fig. 4. SEM micrographs of porous Ni(1:1) (a, b) and Ni(1:4) (d, e) films and the corresponding pore size distributions for Ni(1:1) (c) and Ni(1:4) (f) obtained by micelle-assisted electrodeposition with PS-*b*-P4VP, followed by polymer removal.
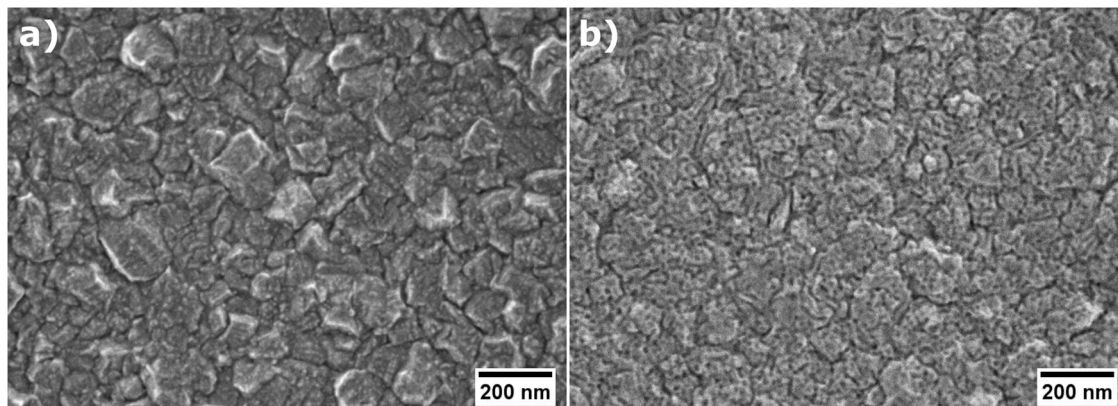

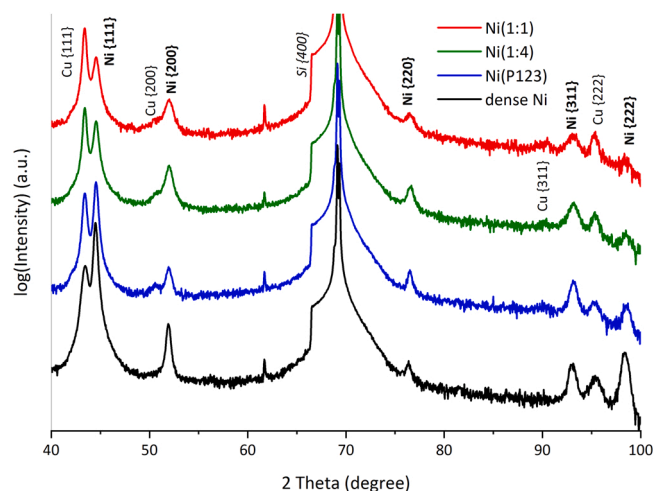**Fig. 5.** SEM micrographs of dense Ni (a) and Ni(P123) (b) films.

Fig. 6. XRD patterns of Ni films deposited by micelle-free (dense film) and micelle-assisted electrodeposition.
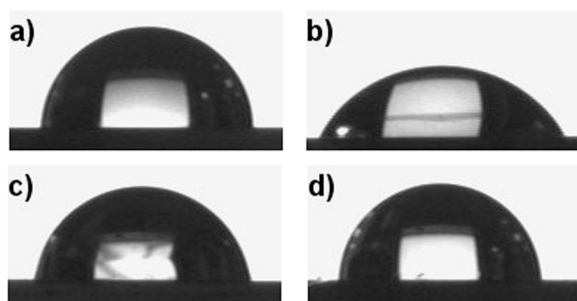

Fig. 7. Contact angle photographs of a droplet of ultrapure water on Ni(1:1) (a), Ni(1:4) (b), Ni(P123) (c), and dense Ni (d) films immediately after deposition of the droplet.

Table 2
Determined water contact angles of Ni films.

	initial CA	CA ($t > 60$ s)
Ni(1:1)	100°	71°
Ni(1:4)	74°	—
Ni(P123)	86°	64°
dense Ni	91°	80°

medium—i. e. an aqueous solution—is slowly added, leading to an arrangement of hydrophobic and hydrophilic polymer chains and hence, the formation of micelles. THF may then be evaporated from the solution. Herein, a similar approach is used with non-commercial polystyrene-poly(4-vinylpyridine) diblock copolymers (PS-*b*-P4VP) synthesised in-house in order to use micelle-assisted electrodeposition for the synthesis of porous Ni films with sub-micrometre pores. The PS-*b*-P4VP BCP is a relatively versatile polymer which can be readily synthesised in a variety of configurations, and allows for the stabilisation of different geometries, including micelles, through different methods [30,31]. In this way, it can serve as a template for the growth of a large variety of nanostructured materials [32,33]. Here, the Ni films synthesised using two different configurations of the BCP are investigated for HER in alkaline media, and compared to mesoporous Ni film with a defined porosity of 10 nm and dense Ni film, likewise obtained from electrodeposition.

2. Material and methods

2.1. Polymerisation of PS-b-P4VP diblock copolymers

The PS-*b*-P4VP BCPs were synthesised by living anionic polymerisation following the methodology described by Varshney et al. [34].

A solution of α-methylstyrene in dry THF (100 ml) was prepared in a three-necked round-bottom flask. Then, the initiator *sec*-butyllithium (1.4 M in cyclohexane) was added dropwise to the solution using a stainless steel syringe until the colour of the solution persisted. After this, the reaction was cooled down to −78 °C and the required amount of the styrene was added slowly. A sudden change of the colour of the initiator was noticed (from red to light yellow). When the solution turned again to intense red, the polymerisation of the P4VP started by addition of 4-vinylpyridine. The polymerisation was terminated by adding methanol, and a milky solution was obtained. Afterwards, the block copolymer was recovered by precipitation in hexane and it was thoroughly dried under vacuum.

The block ratios of PS and P4VP in the block polymers (the ratios of m/n in Fig. 1) were controlled by the amounts of styrene and 4-vinylpyridine used. PS-*b*-P4VP with a block ratio of 1:1 was synthesised using 40 mmol of styrene and 40 mmol of 4-vinylpyridine, while a block ratio of 1:4 was obtained using 17 mmol of styrene and 63 mmol of 4-vinylpyridine (Tab. 1).

The successful polymerisation was verified by ^{1}H NMR (nuclear magnetic resonance) using a Bruker AVANCEII 300 and Bruker Avance DRX 300.

The molecular weights (M_w) of the copolymers were determined by gel permeation chromatography (GPC). The chromatographer was calibrated using standardised samples of PS. The column used was a TSK-GEL G3000H with a pore size of 6 μm. THF was used as eluent, the flow rate was fixed at 1 μl/min, the volume of sample injected in each experiment was 20 μl and the lamp wavelength was set at 254 nm.

2.2. Electrolyte preparation

For the electrodeposition process, a total of four different electrolytes were prepared. Unless otherwise stated, chemicals of analytical grade were used. In addition to the electrolytes containing PS-*b*-P4VP micelles with molecular ratios of 1:1 and 1:4, respectively, an electrolyte containing commercial Pluronic P-123, as well as a micelle-free electrolyte for the deposition of nonporous films were prepared.

A method for the stabilisation of PS-*b*-P4VP micelles of the polymer has previously been developed [32], however, this method had to be merged with the preparation of the electrolyte for electrodeposition. The preparation of PS-*b*-P4VP micelles for the electrolyte was following the methodology described by Artal et al. [29]. 15 mg of the polymer were first dissolved in 5 ml of THF at 50 °C for 24 h. By dropwise addition of 2.5 ml of ethanol and 17.5 ml of ultrapure water, the polymer chains are oriented in a way that the hydrophilic P4VP segments of the polymer are surrounded by water, while the hydrophobic PS segments remain in THF, making up the core of the micelles. To protonate the micelles, the pH was then adjusted to 3.0 by addition of concentrated HCl. In the end, 200 mM NiCl$_2$, 200 mM H$_3$BO$_3$, and 25 mM NH$_4$Cl were dissolved in the micelle-containing solution. The final pH was adjusted to 2.7. The protonation of the micelles in acidic pH guarantees electrostatic repulsion and prohibits agglomeration of micelles. When the Ni(II) species is added, Ni ions are expected to replace protons at the surface of the micelles and ensure successful co-deposition of Ni(0) and micelles as well as the establishment of a continuous Ni(0) matrix in the film during deposition.

For the electrolyte containing P-123 and the micelle-free electrolyte, an aqueous solution of the above quantities of NiCl$_2$, H$_3$BO$_3$, and NH$_4$Cl was prepared. For the P-123 containing electrolyte, 10 mg/ml of the polymer were dissolved in the electrolyte. pH values were adjusted to 2.7 using HCl likewise.
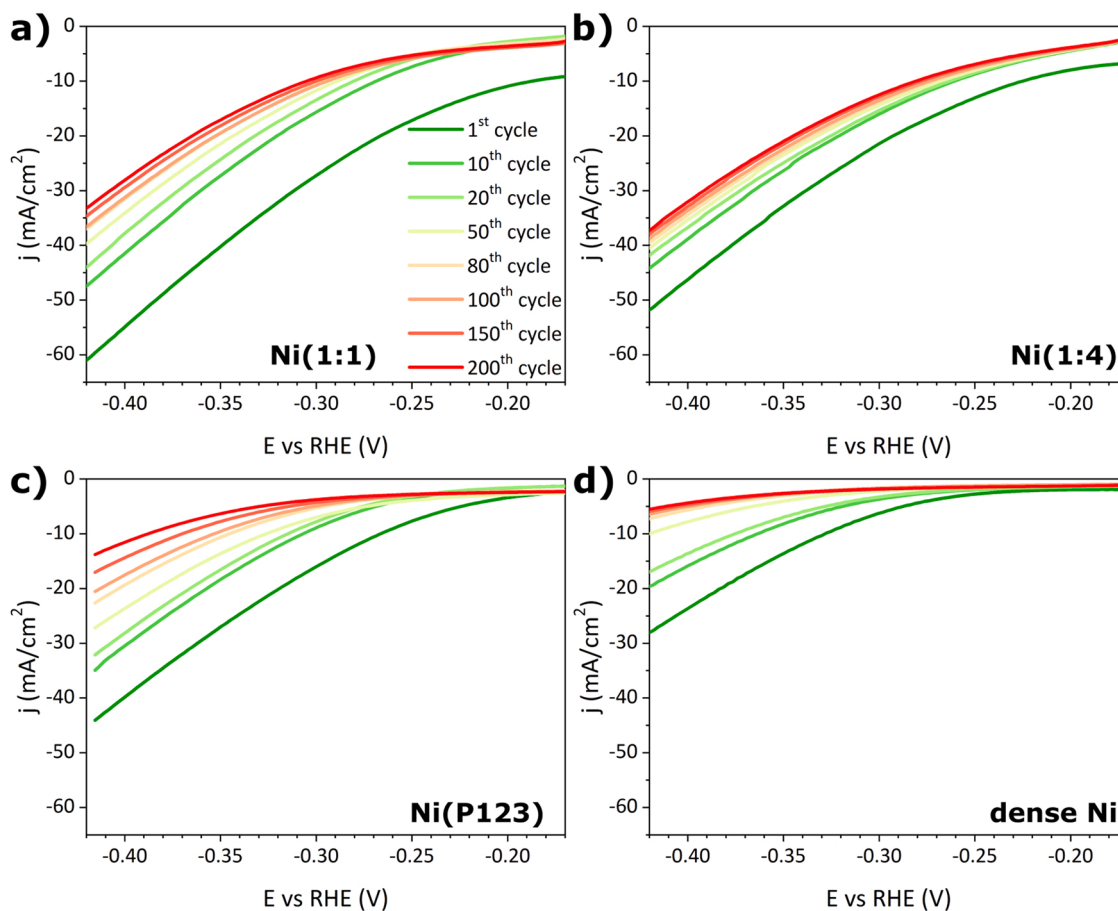
Fig. 8. LSV curves for evaluation of HER recorded in 1 M KOH for a) Ni(1:1), b) Ni(1:4), c) Ni(P123), and d) dense Ni films. Currents are normalised to the geometric area of the electrode.

For simplification, the Ni deposits obtained from their respective electrolytes will be denoted as 'dense' for the micelle-free deposited Ni films, 'Ni(P123)' for the Ni films obtained from the P-123 containing electrolyte, and 'Ni(1:1)' and 'Ni(1:4)' for the Ni films obtained by micelle-assisted electrodeposition using the PS-*b*-P4VP polymer in block ratios of 1:1 and 1:4, respectively.

2.3. Electrodeposition of Ni films

All electrochemical processes were performed using an Autolab 302 N potentiostat controlled by GPES software. Cyclic voltammetries (CV) were run to characterise the baths in order to identify the reduction potential ranges for each electrolyte prior to electrodeposition. A three-electrode set-up was utilised, using a vitreous carbon rod with 3.14 mm^2 working area as the working electrode (WE), a Pt wire as counter electrode, and an Ag|AgCl (3 M KCl) reference electrode. CVs were run from -1.3 V to 1.3 V vs Ag|AgCl under stagnant conditions at a scan rate of 50 mV/s.

The substrates for Ni deposition consisted of silicon wafer material sputter-coated with a thin seed layer of Ti and a Cu layer of approx. 200 nm thickness. Before electrodeposition, the substrates of about 1 cm^2 working area were first cleaned in ethanol in an ultrasonic bath and then activated by submersion in concentrated H_2SO_4(aq) for a few seconds.

The electrodeposition was carried out in the three electrode set-up used for CV, with the metallised silicon substrates as the WE placed vertically in the electrolyte. The deposition was carried out potentiostatically at different cathodic potentials, until an optimum deposition potential was determined for each electrolyte. De-aeration with nitrogen

gas was performed before each deposition, and the deposition was carried out during magnetic stirring at 200 rpm from an electrolyte volume of 25 ml. Finally, Ni(1:1) was deposited at -1.2 V vs Ag|AgCl for 60 s and Ni(1:4) at -1.3 V vs Ag|AgCl for 30 s. Both dense Ni and Ni(P123) were deposited at -1.1 V vs Ag|AgCl for 60 s. Furthermore, for the electrolytes containing PS-*b*-P4VP micelles, the electrodeposition of Ni (1:1) and Ni(1:4) was conducted at a temperature of 50 ˚C, while deposition from the other electrolytes was performed at room temperature.

After the synthesis of the porous Ni films, the micelles were redissolved by immersion of the samples in THF in an ultrasonic bath for 1 h, exchanging the solvent every 20 min, and subsequently a short chemical attack of a few seconds in piranha solution (concentrated solution of H_2SO_4 and H_2O_2 in relation 3:1) was carried out.

2.4. Characterisation

The PS-*b*-P4VP micelles were characterised by transmission electron microscopy (TEM) in order to visualise and confirm their formation and size distribution. Two drops of the micelle solution (before addition of the Ni salt and additives) were deposited onto a copper grid for TEM. The micelles were imaged in a TEM JEOL 1400 with an accelerating voltage of 120 kV.

The electrodeposited Ni films were analysed by scanning electron microscopy (SEM) coupled with energy-dispersive X-ray spectroscopy (EDX) on a Zeiss Merlin electron microscope with an InLens detector at an accelerating voltage of 1 kV. EDX was performed at 20 kV accelerating voltage in order to check the composition of the films. Pore size distributions were determined from the SEM micrographs using the
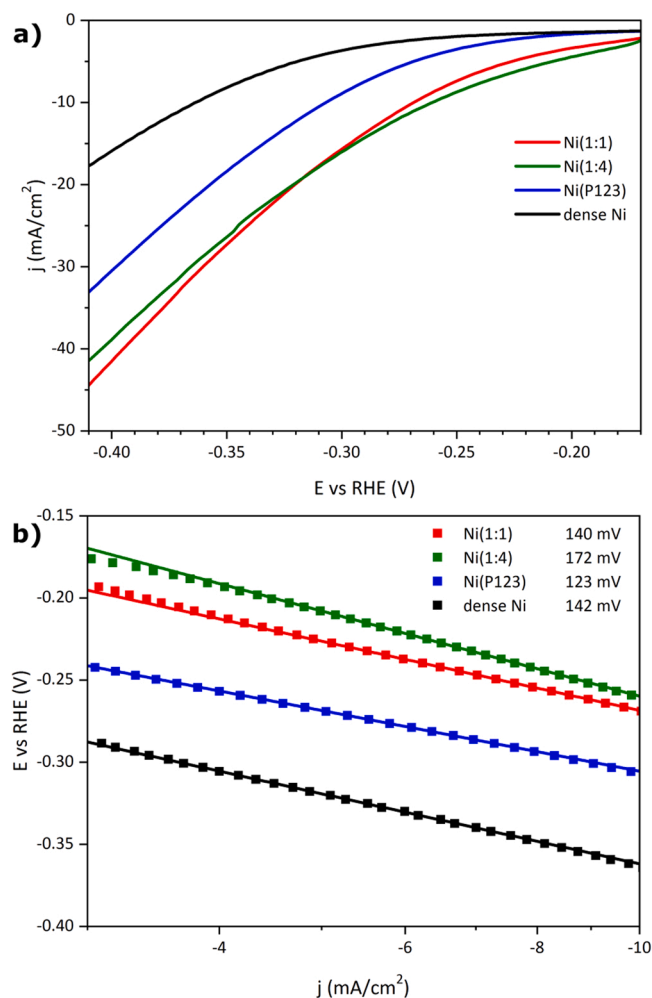
Fig. 9. HER polarisation curves of all Ni films at the 10th sweep (a) and corresponding Tafel slopes (b). Currents are normalised to the geometric surface area of the electrode.

image manipulation software ImageJ.

HER was studied in 1 M KOH solution at room temperature in the same set-up as used for electrodeposition. 200 linear sweep voltammetries were run from a starting potential of −1.20 V down to −1.55 V vs Ag|AgCl at a scan rate of 50 mV/s. The potentials measured against Ag|AgCl were converted to reversible hydrogen electrode (RHE) scale according to the following equation (Eq. 1):

$$E_{RHE} = E_{Ag|AgCl} + 0.059 \text{ pH} + E^0_{Ag|AgCl} \tag{1}$$

where E_{RHE} is the potential vs RHE, $E_{Ag|AgCl}$ the potential measured against Ag|AgCl, and $E^0_{Ag|AgCl}$ the standard electrode potential of the Ag|AgCl reference electrode. The pH of 1 M KOH was considered 14, and $E^0_{Ag|AgCl}$ in 3 M KCl at 25 °C was taken as 0.210 V.

X-ray diffraction measurements were recorded at a 2θ range from 35 to 100°, using CuK$_\alpha$ radiation in order to analyse the composition and crystallographic structure of the Ni deposits. XRD patterns were acquired on a Malvern-PANalytical X'pert Pro MRD diffractometer. Rietveld refinement of the diffraction patterns was performed using the software MAUD developed by Lutterotti [35].

Contact angle measurements were carried out to achieve better understanding of the films wetting behaviour. The experiments were conducted in an ISO 7 clean room on a KRÜSS DSA 100 smartdrop surface analyser. The measurements were done using ultrapure water droplets of 4 μl, taking three measurements on each sample. X-ray

photoelectron spectroscopy (XPS) was conducted using a PHI 5500 spectrometer. Survey spectra and detail spectra of Ni2p, C1s and O1s were collected before and after Ar ion sputtering for 60 s to analyse both the surface as well as the bulk state of the films. The XPS was performed on Ni films both before and after the HER studies.

3. Results and discussion

3.1. Characterisation of PS-b-P4VP block copolymer

The formation of PS-*b*-P4VP was successfully confirmed by ^{1}H NMR, returning the following proton chemical shifts. [(C$_8$H$_8$)$_n$(C$_7$H$_7$N)$_m$] (CDCl$_3$, 300 MHz), δ_H (ppm): 1.30–1.72 (br, 2 H), 1.72–2.30 (m, 4 H), 6.17–6.86 (m, 5 H), 6.86–7.23 (br, 2 H), 8.13–8.63 (m, 2 H).

The molecular weights determined by GPC are 114700 g/mol for PS-*b*-P4VP with a block ratio of 1:1, and 42500 g/mol for the block ratio of 1:4.

3.1.1. PS-b-P4VP micelle formation

The formation of micelles from PS-*b*-P4VP containing solutions was verified by TEM, before the addition of Ni salt and additives. For both configurations of PS-*b*-P4VP, micelles were found on the TEM grid. PS-*b*-P4VP 1:1 micelles were homogeneously distributed on the TEM grid with diameters varying from 20 to 600 nm, while the mean diameter of PS-*b*-P4VP 1:4 micelles is 36 nm (Fig. 2).

3.2. Electrolyte characterisation

The electrolytes were characterised to determine the potential range where the deposition of nickel takes place, and to compare the effects that the different BCPs might produce on the electroreduction process. The micelle-free electrolyte shows the lowest overpotential for the reduction of the Ni(II) species at around −0.7 V (Fig. 3, black curve), as well as the highest reduction current density, suggesting that the deposition rate is also highest in this case. For all micelle-containing electrolytes, the reduction potential is shifted towards more negative potentials. Interestingly, the electrolytes containing PS-*b*-P4VP micelles, despite their higher molecular weight, show an earlier onset of Ni(II) reduction than the P-123 containing electrolyte. This behaviour may hint at a better coordination of Ni(II) ions with PS-*b*-P4VP micelles in comparison to the P-123 micelles. Ni ions may substitute protons on the previously protonated micelles, and the more Ni ions are coordinated with the micelles in relation to the micellar mass, the more positive the reduction potential should be, assuming that the interaction between micelles and Ni ions is not disrupted due to the electric field.

In the anodic scan, two major oxidation peaks are detected for all electrolytes. A peak at 0 V vs Ag|AgCl potential is present in all cases, which partially overlaps with another oxidation peak between 0.2 V and 0.3 V vs Ag|AgCl. The peak at 0 V is attributed to the oxidation of adsorbed hydrogen, while at more positive potentials, oxidation may be attributed to the formation of Ni(OH)$_2$ and further oxidation to NiOOH [36,37]. The double peak is also observed in the oxidation response of Ni (P123), although slightly shifted towards more cathodic potentials (see inset in Fig. 3).

3.3. Morphology of the Ni films

Highly porous Ni films were successfully obtained by micelle-assisted electrodeposition using PS-*b*-P4VP with different molar ratios of the blocks PS:P4VP (concretely, 1:1 and 1:4) after removal of the polymer (Fig. 4). Spherical pores, ranging from mesoporous to macroporous range, are homogeneously distributed across the surface of the films. Ni(1:1) shows a higher spread in pore size with respect to Ni(1:4); ranging from 25 nm to 600 nm for Ni(1:1), and from 10 nm to 230 nm for Ni(1:4). Due to the short chemical attack with piranha solution for removal of the micelles, the Ni films are also slightly etched; this effect is
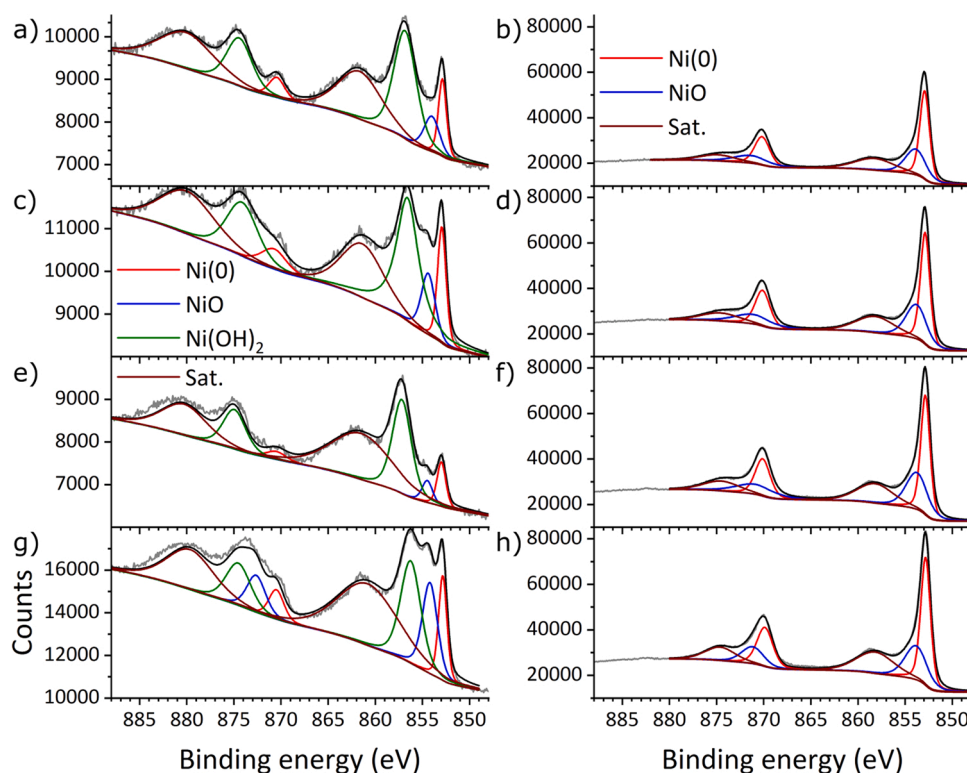
Fig. 10. Ni2p core-level XPS surface spectra before (left) and after Ar ion sputtering for 60 s (right) for Ni(1:1) (a, b), Ni(1:4) (c, d), Ni(P123) (e, f), and dense Ni film (g, h). All spectra were collected before HER in alkaline media.
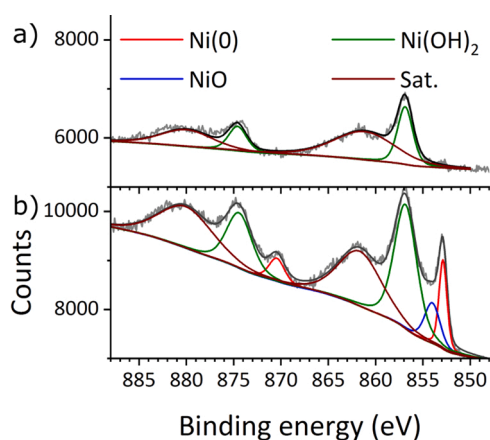
Fig. 11. Ni2p core-level XPS surface spectra for Ni(1:1) after 200 LSVs of HER in alkaline media (a) and in initial state (b).

more pronounced for Ni(1:1). At large magnification, sub-surface porosity and in some cases even the substrate layer become visible, showing that the porosity is interconnected and therefore leads to a very high S/V (Fig. 4b and e). While the pore sizes appear rather randomly distributed for Ni(1:1), Ni(1:4) shows a large number of finely distributed mesopores in addition to randomly spread larger pores. In statistical terms, this results in a much narrower pore size distribution for Ni (1:4) (note the difference in pore size range and intervals between Fig. 4c and f).

From the resulting pore sizes and their distributions it can be inferred that the PS-*b*-P4VP with 1:4 ratio, containing larger hydrophilic P4VP block chains, leads to better stabilisation and separation of the micelles. The PS-*b*-P4VP polymer with a lower content of hydrophilic groups (PS/ P4VP ratio of 1:1) led to the formation of many larger micelles,

presumably due to higher interactions of the polymer chains due to insufficient hydrophilicity, thus the assembly into larger micelles. However, even though a higher number of hydrophilic components seems to lead to a more well-defined pore size distribution, the randomly distributed pore size of Ni(1:1) appears more promising as an electrocatalyst in terms of S/V.

The Ni(P123) and dense Ni films synthesised for comparison show a very similar fine-grained structure. In addition, Ni(P123) very clearly shows a highly mesoporous surface with a narrowly distributed pore size of 10 nm (Fig. 5). However, an interconnection of the mesopores in Ni (P123) is not appreciable from the on-top SEM images.

3.3.1. Structural analysis

The X-ray diffractograms show all diffraction peaks for face-centred cubic (fcc) Ni for all four configurations, demonstrating that the Ni deposits are polycrystalline (Fig. 6). A specific texture is not apparent. Apart from Si and Cu reflections originating from the substrate materials, no other phases, such as Ni oxides or hydroxides, are detected by XRD. An additional, narrow peak at 62° present in all spectra could not be identified and may be an artefact coming from the sample holder.

The main apparent difference between the different Ni films is that the diffraction peaks of the dense film are narrower than those of the films produced by micelle-assisted deposition. This observation is most apparent at the Ni{200} reflection. The crystal sizes obtained by Rietveld refinement are 75 nm for the dense Ni film and 52 nm for Ni(P123); these values correspond rather well with the grain sizes observed by SEM (cf. Fig. 5). When the high molecular weight PS-*b*-P4VP polymers were used in the synthesis, the crystal size was further reduced to 27 nm for Ni(1:1) and 25 nm for Ni(1:4). It is conjectured that this smaller grain size is the result of an interference of the polymeric micelles with the crystal growth during deposition.

3.3.2. Contact angle measurements

For electrocatalysis in aqueous media such as the HER, a good

wetting behaviour is a necessity because the entire surface needs to be in contact with the electrolyte in order to completely benefit from the high S/V. Since porous materials often exhibit hydrophobic surface properties, the wettability of the porous Ni films needs to be investigated.

Initially, the highest water contact angle was found for Ni(1:1) with a mean value of 100° (Fig. 7). However, a strong time dependence of the contact angle was observed on the porous films during the measurements, where the contact angle gradually decreased over time (Tab. 2). After one minute, the contact angles of the porous films are significantly lower than initially. In the case of Ni(1:4), this process was much faster and the contact angle decreased rapidly in just a few seconds. This time dependence may also be an indicator that the water penetrates the openly porous structure; in fact, a loss in volume could be confirmed for Ni(1:1) through a reduction of the cross-section of a droplet of 17% within a minute, along with the reduction of the contact angle from 93° to 63°. The observed difference in time dependence may be related to the difference in pore size distribution. Under the assumption that large pores are filled immediately by water and do not contribute to the time dependence, then there is a lower amount of small pores available in Ni(1:1), while the large amount of small pores in Ni(1:4) facilitates a faster penetration of the water through the porous structure.

The dense Ni film yielded a mean contact angle of 91°, in comparison to the porous films this angle remained relatively stable and only decreased slowly until 80° at the end of the experiment. Ni(P123) shows the best wettability after one minute, which may also be caused by the soap-like behaviour of possible remnants of the BCP. After all, the contact angle measurements demonstrate a hydrophilic behaviour of the porous Ni films with improved wettability with respect to the dense film.

3.3.3. Hydrogen evolution reaction in alkaline media

The LSV curves recorded to assess the HER activity of the films show that the openly porous Ni films prepared using PS-*b*-P4VP micelles exhibit significantly higher HER activity than the dense film and Ni(P123), initially being about 60% higher with respect to the dense Ni film (Fig. 8). In turn, Ni(P123) exhibits a 49% improvement with respect to the dense film. All Ni films experienced a loss in the electrocatalytic activity upon cycling. Comparing the first and 200th sweep at a potential of -0.4 V vs RHE, shows that the dense Ni film exhibits a decrease in cathodic current density of over 20 mA/cm^2 (around 75%), Ni(1:1) shows a decrease of over 25 mA/cm^2 (around 40%), and Ni(1:4) has the lowest loss in electrocatalytic activity, namely 14 mA/cm^2 (around 25%). Meanwhile, Ni(P123) showed a decrease of over 30 mA/cm^2 (around 70%). According to these data, both Ni(1:1) and Ni(1:4) showed significant improvement in electrocatalytic stability compared to dense Ni and Ni(P123). Due to this difference in stability, after 200 sweeps the catalytic activity of both Ni(1:1) and Ni(1:4) is over three times higher than the activity of the dense Ni film.

The direct comparison of electrocatalytic activity is observed by comparing the 10th sweep for each electrocatalyst (Fig. 9a). In this view it is not only clear that the Ni films produced using PS-*b*-P4VP micelles yield higher HER current densities, but also that the onset overpotential is shifted towards more positive potentials. In terms of kinetics, which are evaluated based on the determined Tafel slope *b*, there are rather little differences. The lowest Tafel slope is found for Ni(P123) with 123 mV. Ni(1:1) and the dense Ni films have almost identical Tafel slopes with 140 mV and 142 mV, respectively. Ni(1:4) has the highest Tafel slope with 172 mV and therefore slower kinetics, however, this film exhibits the lowest overpotential at low current densities (Fig. 9b). The Tafel slopes are close to what has been reported for pure Ni, suggesting that HER follows the Volmer-Heyrosvky mechanism, the latter being the rate-determining step [38].

3.4. Chemical state of the electrodeposited films before and after HER

All electrodeposited Ni films show surfaces containing mostly metallic Ni at 853 eV as well as oxidised Ni(II) species at 857 eV which can be attributed to the presence of Ni(OH)$_2$ [39,40]. Ni(P123) shows the lowest fraction of metallic Ni. In addition, the dense Ni film shows a rather large contribution of oxidised Ni species at 854 eV, attributed to NiO (Fig. 10).

After sputtering, the Ni2p photoelectron spectra do not show any significant differences between the Ni films obtained from the different electrolytes. A difference in intensity is appreciated due to the variation in porosity. Other than that, the electrodeposited films consist mostly of metallic Ni, in addition to a minor fraction of oxidised Ni.

After the HER measurements, the surfaces do not show any contribution of metallic Ni. Instead, Ni(OH)$_2$ has formed on the surface, as shown exemplarily for Ni(1:1) (Fig. 11). Therefore, the metallic Ni films' surfaces are oxidised to Ni(OH)$_2$ during HER and the electrocatalytically active species change from contributions of metallic Ni and Ni(OH)$_2$ to Ni(OH)$_2$ only. This passivation also explains the initial decrease in HER activity, since, in direct comparison metallic Ni shows superior activity over Ni(OH)$_2$ [21]. However, Ni(OH)$_2$ should provide a sufficiently stable surface for long-term performance in alkaline media.

Taking into account all of the obtained results, the openly porous Ni films prepared by micelle-assisted electrodeposition using PS-*b*-P4VP show a clear improvement in hydrogen evolution activity over mesoporous Ni(P123) and dense Ni films. This improvement cannot be referred to any chemical or crystallographic differences, so that it is mainly related to the significantly higher surface areas resulting from the openly porous microstructures of Ni(1:1) and Ni(1:4). In HER, the open porosity, combined with the good wetting behaviour of the films, theoretically allows for complete exploitation of the porosity because movement of electrolyte and gases is promoted. In an openly porous structure, the electrolyte can penetrate the structure while the formed hydrogen can escape through different channels in absence of capillary forces.

Furthermore, the openly porous Ni films do not only display higher HER performance than the dense and mesoporous films, but also a lower loss in electrocatalytic activity over time, leading to an activity at HER which is a factor 3 higher at end of test. This observation seems surprising since the material itself is essentially the same, and the only structural difference is in the crystal size. Even though Ni(P123) shows lower amounts of metallic Ni at the surface, which may be deleterious for the initial catalytic activity, all Ni films' surfaces are covered by hydroxides after HER, as observed by XPS. Possible differences are in the thickness of the hydroxide layer, since a relatively thin hydroxide layer on top of the metallic Ni should be advantageous for HER due to better conductivity. The formation of the hydroxide may very well have been influenced by the crystal size of the Ni films [41]. Judging from the structure of PS-*b*-P4VP, it is also thinkable that nitrogen may have been incorporated into the Ni films, which may have limited the growth of the hydroxide.

Since the wetting behaviour is seen to be time-dependent, it is possible that the alkaline electrolyte still continues to wet, i. e. to penetrate the porous structure during the tests, so that the surface area in contact with the electrolyte is slowly increasing. The fact that both Ni(1:1) and Ni(1:4), despite their apparent difference in pore size distribution, exhibit rather similar activity at HER, leads to the conclusion that the crucial property of the porous films is in fact their interconnected porosity; the actual size and distribution of pores seems to have only minor influence. The initial loss of electrocatalytic activity is attributed to the superficial oxidation of metallic Ni to Ni(OH)$_2$, as confirmed by XPS.

Chen et al. obtained a high-surface-area Ni electrode by synthesis of Ni nanowires, reaching an improvement of factor 7 at HER in neutral electrolyte with respect to a planar Ni electrode [42]. The Tafel slopes determined here are comparable to those of different Raney nickel-aluminium-molybdenum alloys determined in 1 M KOH, although those exhibit lower overpotentials [43], and Pt-decorated Ni electrodes [44]. The Tafel slopes determined here are also considerably lower than those obtained by Qian et al. on electrodeposited porous Ni

electrodes in 30 wt% KOH which, in agreement with our results, show an initial loss in activity during galvanostatic long-term electrolysis, but a rather high stability afterwards [45]. This passivation effect is common and has been observed for different Ni-based alloys, irrespective of the synthesis method [12,46].

4. Conclusions

PS-*b*-P4VP BCP micelles with two different block ratios (PS to P4VP ratios of 1:1 and 1:4) were successfully prepared in an electrolyte for use in micelle-assisted electrodeposition of Ni films. The Ni films produced in this way are highly porous with a rather large distribution in pore size ranging from the mesoporous to the macroporous range. The achieved porosity is well defined, with spherically shaped pores homogeneously distributed throughout the samples.

In view of the electrocatalytic activity at HER, the significant improvement in activity of both Ni(1:1) and Ni(1:4) over mesoporous Ni (P123) shows that the open porosity and the larger pore size is much favourable for hydrogen evolution, and supports the supposition that mesopores with 10 nm in diameter, as for Ni(P123), do not allow for sufficient penetration of the aqueous media either due to their size or due to the fact that they are not fully interconnected.

The demonstrated synthesis process adds a new dimension to electrodeposition and its versatility to synthesise different nano- and microstructures. What has been shown for Ni films, can be readily adopted to other metals and alloys commonly obtained by electrodeposition, as long as all species are chemically compatible with the BCP. This opens new possibilities, not only for the field of electrocatalysis, but also for many other fields where porous and high surface area materials are of interest, such as batteries, electrochemical supercapacitors, water remediation, or drug delivery.

CRediT authorship contribution statement

Roberto Fagotto Clavijo: Methodology, Validation, Formal analysis, Investigation, Data curation, Writing – original draft, Visualization. **Marta Riba-Moliner**: Validation, Resources, Writing – review & editing. **Arántzazu González-Campo:** Validation, Resources, Writing – review & editing. **Jordi Sort**: Resources, Writing – review & editing, Funding acquisition. **Eva Pellicer**: Conceptualization, Validation, Resources, Writing – review & editing, Supervision, Project administration, Funding acquisition. **Konrad Eiler**: Conceptualization, Formal analysis, Writing – review & editing, Visualization, Supervision.

Declaration of Competing Interest

The authors declare that they have no known competing financial interests or personal relationships that could have appeared to influence the work reported in this paper.

Data availability

Data will be made available on request.

References

[1] P. di Sia, Hydrogen and the state of art of fuel cells, J. Nanosci. Adv. Technol. 2 (2018) 6, https://doi.org/10.24218/jnat.2017.27.

[2] I. Staffell, D. Scamman, A. Velazquez Abad, P. Balcombe, P.E. Dodds, P. Ekins, N. Shah, K.R. Ward, The role of hydrogen and fuel cells in the global energy system, Energy Environ. Sci. 12 (2019) 463, https://doi.org/10.1039/C8EE01157E.

[3] K.T. Møller, T.R. Jensen, E. Akiba, H.-W. Li, Hydrogen - a sustainable energy carrier, Prog. Nat. Sci. 27 (2017) 34, https://doi.org/10.1016/j.pnsc.2016.12.014.

[4] T. Tsoutsos, Hybrid wind-hydrogen energy systems, in: J.K. Kaldellis (Ed.), Stand-Alone and Hybrid Wind Energy Systems, Elsevier, 2010, pp. 254–281, https://doi.org/10.1533/9781845699628.2.254.

[5] A.S. Aricò, P. Bruce, B. Scrosati, J.-M. Tarascon, W. van Schalkwijk, Nanostructured materials for advanced energy conversion and storage devices, Nat. Mater. 4 (2005) 366, https://doi.org/10.1038/nmat1368.

[6] M. Bernal Lopez, J. Ustarroz, Electrodeposition of nanostructured catalysts for electrochemical energy conversion: Current trends and innovative strategies, Curr. Opin. Electrochem 27 (2021), 100688, https://doi.org/10.1016/j.coelec.2021.100688.

[7] F. Liu, C. Shi, X. Guo, Z. He, L. Pan, Z.-F. Huang, X. Zhang, J.-J. Zou, Rational design of better hydrogen evolution electrocatalysts for water splitting: A review, Adv. Sci. 9 (2022), 2200307, https://doi.org/10.1002/advs.202200307.

[8] J. Zhang, A. Quintana, E. Menéndez, M. Coll, E. Pellicer, J. Sort, Electrodeposited Ni-based magnetic mesoporous films as smart surfaces for atomic layer deposition: an "all-chemical" deposition approach toward 3D nanoengineered composite layers, ACS Appl. Mater. Interfaces 10 (2018) 14877, https://doi.org/10.1021/acsami.8b01626.

[9] K. Eiler, S. Suriñach, J. Sort, E. Pellicer, Mesoporous Ni-rich Ni–Pt thin films: electrodeposition, characterization and performance toward hydrogen evolution reaction in acidic media, Appl. Catal. B 265 (2020), 118597, https://doi.org/10.1016/j.apcatb.2020.118597.

[10] W.L. Tsai, P.C. Hsu, Y. Hwu, C.H. Chen, L.W. Chang, J.H. Je, H.M. Lin, A. Groso, G. Margaritondo, Building on bubbles in metal electrodeposition, Nature 417 (2002) 139, https://doi.org/10.1038/417139a.

[11] R. Andaveh, G.B. Darband, M. Maleki, A.S. Rouhaghdam, Superaerophobic/superhydrophilic surfaces as advanced electrocatalysts for the hydrogen evolution reaction: a comprehensive review, J. Mater. Chem. A 10 (2022) 5147, https://doi.org/10.1039/d1ta10519a.

[12] Y.-J. Huang, C.-H. Lai, P.-W. Wu, L.-Y. Chen, Ni inverse opals for water electrolysis in an alkaline electrolyte, J. Electrochem. Soc. 157 (2010) P18, https://doi.org/10.1149/1.3281332.

[13] M. Metikoš-Huković, Z. Grubač, N. Radić, A. Tonejc, Sputter deposited nanocrystalline Ni and Ni-W films as catalysts for hydrogen evolution, J. Mol. Catal. A 249 (2006) 172, https://doi.org/10.1016/j.molcata.2006.01.020.

[14] J. Zhang, M.D. Baró, E. Pellicer, J. Sort, Electrodeposition of magnetic, superhydrophobic, non-stick, two-phase Cu-Ni foam films and their enhanced performance for hydrogen evolution reaction in alkaline water media, Nanoscale 6 (2014) 12490, https://doi.org/10.1039/c4nr03200d.

[15] Z. Feng, H. Zhang, B. Gao, P. Lu, D. Li, P. Xing, Ni-Zn nanosheet anchored on rGO as bifunctional electrocatalyst for efficient alkaline water-to-hydrogen conversion via hydrazine electrolysis, Int. J. Hydrog. Energy 45 (2020) 19335, https://doi.org/10.1016/j.ijhydene.2020.05.120.

[16] L. Shang, Y. Zhao, X.-Y. Kong, R. Shi, G.I.N. Waterhouse, L. Wen, T. Zhang, Underwater superaerophobic Ni nanoparticle-decorated nickel-molybdenum nitride nanowire arrays for hydrogen evolution in neutral media, Nano Energy 78 (2020), 105375, https://doi.org/10.1016/j.nanoen.2020.105375.

[17] A. Modak, R. Mohan, K. Rajavelu, R. Cahan, T. Bendikov, A. Schechter, Metal-organic polymer-derived interconnected Fe–Ni alloy by carbon nanotubes as an advanced design of urea oxidation catalysts, ACS Appl. Mater. Interfaces 13 (2021) 8461, https://doi.org/10.1021/acsami.0c22148.

[18] R. Mohan, A. Modak, P. Subramanian, R. Cahan, P. Sivakumar, A. Gedanken, A. Schechter, Electrochemical oxidation of glycine with bimetallic nickel-manganese oxide catalysts, ChemElectroChem 7 (2020) 561, https://doi.org/10.1002/celc.201901996.

[19] S. Marini, P. Salvi, P. Nelli, R. Pesenti, M. Villa, M. Berrettoni, G. Zangari, Y. Kiros, Advanced alkaline water electrolysis, Electrochim. Acta 82 (2012) 384, https://doi.org/10.1016/j.electacta.2012.05.011.

[20] Y. Ito, M. Izumi, D. Hojo, M. Wakisaka, T. Aida, T. Adschiri, One-step nanoporous structure formation using NiO nanoparticles: Pore size control and pore size dependence of hydrogen evolution reaction, Chem. Lett. 46 (2017) 267, https://doi.org/10.1246/cl.161017.

[21] Z. Xing, L. Gan, J. Wang, X. Yang, Experimental and theoretical insights into sustained water splitting with an electrodeposited nanoporous nickel hydroxide@ nickel film as an electrocatalyst, J. Mater. Chem. A 5 (2017) 7744, https://doi.org/10.1039/C7TA01907F.

[22] X. Yu, J. Zhao, L.-R. Zheng, Y. Tong, M. Zhang, G. Xu, C. Li, J. Ma, G. Shi, Hydrogen evolution reaction in alkaline media: Alpha- or beta-nickel hydroxide on the surface of platinum? ACS Energy Lett. 3 (2018) 237, https://doi.org/10.1021/acsenergylett.7b01103.

[23] B. Liu, C. Wu, G. Chen, W. Chen, L. Peng, Y. Yao, Z. Wei, H. Zhu, T. Han, D. Tang, M. Zhou, All-in-one surface engineering strategy on nickel phosphide arrays towards a robust electrocatalyst for hydrogen evolution reaction, J. Power Sources 429 (2019) 46, https://doi.org/10.1016/j.jpowsour.2019.04.119.

[24] P.A. Nelson, J.M. Elliott, G.S. Attard, J.R. Owen, Mesoporous nickel/nickel oxide—a nanoarchitectured electrode, Chem. Mater. 14 (2002) 524, https://doi.org/10.1021/cm011021a.

[25] R. Nagarajan, "Non-equilibrium" block copolymer micelles with glassy cores: a predictive approach based on theory of equilibrium micelles, J. Colloid Interface Sci. 449 (2015) 416, https://doi.org/10.1016/j.jcis.2014.12.077.

[26] Y. Yamauchi, A. Sugiyama, R. Morimoto, A. Takai, K. Kuroda, Mesoporous platinum with giant mesocages templated from lyotropic liquid crystals consisting of diblock copolymers, Angew. Chem. 47 (2008) 5371, https://doi.org/10.1002/anie.200801381.

[27] D. Baba, J. Kim, J. Henzie, C. Li, B. Jiang, Ö. Dag, Y. Yamauchi, T. Asahi, Electrochemical deposition of large-sized mesoporous nickel films using polymeric micelles, Chem. Commun. 54 (2018) 10347, https://doi.org/10.1039/C8CC04070B.

[28] C. Li, B. Jiang, Z. Wang, Y. Li, M.S.A. Hossain, J.H. Kim, T. Takei, J. Henzie, Ö. Dag, Y. Bando, Y. Yamauchi, First synthesis of continuous mesoporous copper films with uniformly sized pores by electrochemical soft templating, Angew. Chem. 128 (2016) 12938, https://doi.org/10.1002/ange.201606031.

[29] R. Artal, A. Serrà, J. Michler, L. Philippe, E. Gómez, Electrodeposition of mesoporous Ni-rich Ni-Pt films for highly efficient methanol oxidation, Nanomaterials 10 (2020) 1435, https://doi.org/10.3390/nano10081435.

[30] S. O'Driscoll, G. Demirel, R.A. Farrell, T.G. Fitzgerald, C. O'Mahony, J.D. Holmes, M.A. Morris, The morphology and structure of PS-b-P4VP block copolymer films by solvent annealing: effect of the solvent parameter, Polym. Adv. Technol. 22 (2009) 915, https://doi.org/10.1002/pat.1596.

[31] A. Rahikkala, A.J. Soininen, J. Ruokolainen, R. Mezzenga, J. Raula, E.I. Kauppinen, Self-assembly of PS-b-P4VP block copolymers of varying architectures in aerosol nanospheres, Soft Matter 9 (2013) 1492, https://doi.org/10.1039/c2sm26913a.

[32] M. Riba-Moliner, C. Oliveras-González, D.B. Amabilino, A. González-Campo, Supramolecular block copolymers incorporating chiral andachiral chromophores for the bottom-up assembly of nanomaterials, J. Porphyr. Phthalocyanines 23 (2019) 916, https://doi.org/10.1142/S1088424619500809.

[33] H.-Y. Si, J.-S. Chen, G.-M. Chow, A simple method to prepare highly ordered PS-b-P4VP block copolymer template, Colloids Surf. A 373 (2011) 82, https://doi.org/10.1016/j.colsurfa.2010.10.034.

[34] S.K. Varshney, X.F. Zhong, A. Eisenberg, Anionic homopolymerization and block copolymerization of 4-vinylpyridine and its investigation by high-temperature size-exclusion chromatography in *N*-methyl-2-pyrrolidinone, Macromolecules 26 (1993) 701, https://doi.org/10.1021/ma00056a022.

[35] L. Lutterotti, Total pattern fitting for the combined size-strain-stress-texture determination in thin film diffraction, Nucl. Instrum. Methods Phys. Res. B 268 (2010) 334, https://doi.org/10.1016/j.nimb.2009.09.053.

[36] M. Vuković, Voltammetry and anodic stability of a hydrous oxide film on a nickel electrode in alkaline solution, J. Appl. Electrochem. 24 (1994) 878, https://doi.org/10.1007/BF00348775.

[37] K. Eiler, H. Krawiec, I. Kozina, J. Sort, E. Pellicer, Electrochemical characterisation of multifunctional electrocatalytic mesoporous Ni-Pt thin films in alkaline and acidic media, Electrochim. Acta 359 (2020), 136952, https://doi.org/10.1016/j.electacta.2020.136952.

[38] N. Krstajić, M. Popović, B. Grgur, M. Vojnović, D. Šepa, On the kinetics of the hydrogen evolution reaction on nickel in alkaline solution. Part I. The mechanism, J. Electroanal. Chem. 512 (2001) 16, https://doi.org/10.1016/S0022-0728(01)00590-3.

[39] L. Salvati, L.E. Makovsky, J.M. Stencel, F.R. Brown, D.M. Hercules, Surface spectroscopic study of tungsten-alumina catalysts using X-ray photoelectron, ion scattering, and Raman spectroscopies, J. Phys. Chem. 85 (1981) 3700, https://doi.org/10.1021/j150624a035.

[40] H.-W. Hoppe, H.-H. Strehblow, XPS and UPS examinations of the formation of passive layers on Ni in 1 M sodium hydroxide and 0.5 M sulphuric acid, Surf. Interface Anal. 14 (1989) 121, https://doi.org/10.1002/sia.740140305.

[41] J.L. Weininger, M.W. Breiter, Effect of crystal structure on the anodic oxidation of nickel, J. Electrochem. Soc. 110 (1963) 484, https://doi.org/10.1149/1.2425798.

[42] P.-C. Chen, Y.-M. Chang, P.-W. Wu, Y.-F. Chiu, Fabrication of Ni nanowires for hydrogen evolution reaction in a neutral electrolyte, Int. J. Hydrog. Energy 34 (2009) 6596, https://doi.org/10.1016/j.ijhydene.2009.05.126.

[43] L. Birry, A. Lasia, Studies of the hydrogen evolution reaction on Raney nickel-molybdenum electrodes, J. Appl. Electrochem. 34 (2004) 735, https://doi.org/10.1023/B:JACH.0000031161.26544.6a.

[44] S. Fiameni, I. Herraiz-Cardona, M. Musiani, V. Pérez-Herranz, L. Vázquez-Gómez, E. Verlato, The HER in alkaline media on Pt-modified three-dimensional Ni cathodes, Int. J. Hydrog. Energy 37 (2012) 10507, https://doi.org/10.1016/j.ijhydene.2012.04.100.

[45] X. Qian, T. Hang, S. Shanmugam, M. Li, Decoration of micro-/nanoscale noble metal particles on 3D porous nickel using electrodeposition technique as electrocatalyst for hydrogen evolution reaction in alkaline electrolyte, ACS Appl. Mater. Interfaces 7 (2015) 15716, https://doi.org/10.1021/acsami.5b00679.

[46] R. Bodnarova, M. Kozejova, V. Latyshev, S. Vorobiov, M. Lisnichuk, H. You, M. Gregor, V. Komanicky, Study of synergistic effects and compositional dependence of hydrogen evolution reaction on MoxNiy alloy thin films in alkaline media, Mol. Catal. 528 (2022), 112481, https://doi.org/10.1016/j.mcat.2022.112481.